AGU PUBLICATIONS

JGR

Journal of Geophysical Research: Space Physics

RESEARCH ARTICLE
10.1002/2017JA024525

Special Section:
Magnetospheric Multiscale (MMS) Mission Results Throughout the First Primary Mission Phase

# Differing Properties of Two Ion-Scale Magnetopause Flux Ropes

L. Alm[1], C. J. Farrugia[1], K. W. Paulson[1], M. R. Argall[1], R. B. Torbert[1,2], J. L. Burch[2], R. E. Ergun[3], C. T. Russell[4], R. J. Strangeway[4], Y. V. Khotyaintsev[5], P.-A. Lindqvist[6], G. T. Marklund[6], and B. L. Giles[7]

[1]Space Science Center, University of New Hampshire, Durham, NH, USA, [2]Southwest Research Institute, San Antonio, TX, USA, [3]Laboratory for Atmospheric and Space Physics, University of Colorado Boulder, Boulder, CO, USA, [4]IGPP/EPSS, University of California Los Angeles, Los Angeles, CA, USA, [5]IRF Swedish Institute of Space Physics Uppsala, Uppsala, Sweden, [6]Department of Space and Plasma Physics, KTH Royal Institute of Technology, Stockholm, Sweden, [7]NASA Goddard Space Flight Center, Greenbelt, MD, USA

**Key Points:**
- The first flux rope exhibits demagnetized ions, strong variable currents, and energy conversion
- The second flux rope has magnetized ions; weak, stable currents; and little energy conversion
- The dynamic behavior of the first flux rope is consistent with results from simulations of flux rope coalescence

**Correspondence to:**
L. Alm,
love@spam.sr.unh.edu

**Citation:**
Alm, L., Farrugia, C. J., Paulson, K. W., Argall, M. R., Torbert, R. B., Burch, J. L., … Giles, B. L. (2018). Differing properties of two ion-scale magnetopause flux ropes. *Journal of Geophysical Research: Space Physics*, *123*, 114–131. https://doi.org/10.1002/2017JA024525

Received 27 JUN 2017
Accepted 28 NOV 2017
Accepted article online 7 DEC 2017
Published online 4 JAN 2018



**Abstract** In this paper, we present results from the Magnetospheric Multiscale constellation encountering two ion-scale, magnetopause flux ropes. The two flux ropes exhibit very different properties and internal structure. In the first flux rope, there are large differences in the currents observed by different satellites, indicating variations occurring over sub-$d_i$ spatial scales, and time scales on the order of the ion gyroperiod. In addition, there is intense wave activity and particle energization. The interface between the two flux ropes exhibits oblique whistler wave activity. In contrast, the second flux rope is mostly quiescent, exhibiting little activity throughout the encounter. Changes in the magnetic topology and field line connectivity suggest that we are observing flux rope coalescence.

## 1. Introduction

Magnetic flux ropes are two-component magnetic field structures consisting of an axial field and an azimuthal field. Flux ropes are used to model phenomena such as flux transfer events (FTEs), observed in the dayside magnetopause, or the three-dimensional equivalents of the magnetic islands and plasmoids observed in the magnetotail. In the elbow-shaped flux ropes, first described by Russell and Elphic (1978) in association with FTEs, the azimuthal field arises from unreconnected field lines wrapped around the flux rope core. Since $B_N$ is continuous and nonzero inside the elbow-shaped flux rope, the magnetic field must be helical rather than arising exclusively from field line draping (Cowley, 1982; Paschmann et al., 1982; Sonnerup, 1987). Flux ropes can also be used to describe magnetic islands generated between multiple X lines (Lee & Fu, 1985). One feature which distinguishes multiple X line flux ropes from elbow-shaped flux ropes is that the multiple X line model allows for any number of flux ropes to be generated, whereas the elbow-shaped flux ropes appear in pairs with one magnetosheath and one magnetospheric branch (Fear et al., 2008).

In addition to macroscopic flux ropes, particle-in-cell (PIC) simulations have shown that a finite guide field can cause the electron current layer to lengthen and thus become unstable to the tearing mode instability, forming numerous small-scale flux ropes, or secondary islands (Daughton et al., 2011; Drake, Swisdak, Schoeffler, et al., 2006). In addition, electron flow along the separatrices can create sufficient flow shear to drive an electron Kelvin-Helmholtz instability, forming electron flow vortices which over time can evolve into secondary flux ropes (Fermo et al., 2012).

Simulations of flux rope formation indicate that we should expect to observe numerous small-scale flux ropes, whereas observational statistics favor macroscopic flux ropes with a scale size of over 2000 km (Fermo et al., 2011). This discrepancy could in part be explained by the observational constraints of past missions favoring macroscopic flux ropes.

These numerous secondary flux ropes can be highly active and can both split into new flux ropes as well as merge with other flux ropes, introducing plasma turbulence. The presence and evolution of these secondary flux ropes has been suggested to play an important role in modifying the reconnection rate (Daughton et al., 2006; Karimabadi et al., 2007; Uzdensky et al., 2010) and drive particle energization (Chen et al., 2008; Drake, Swisdak, Che, & Shay, 2006).

While flux rope coalescence is a well-established idea, there are few direct observations of the process in action. Flux rope coalescence has been observed in the magnetotail by the Cluster satellites, where 63% of the flux ropes observed inside the ion diffusion region were reported to be undergoing coalescence (Wang et al., 2016). Cluster observations have indicated that magnetotail flux ropes exhibiting enhanced core field and decreased core density may have recently undergone coalescence (Retinò et al., 2008). These results have been replicated in PIC simulations, where the two secondary flux ropes, originally exhibiting a core density enhancement, merged into a larger flux rope exhibiting a core density depletion (Zhou et al., 2014). The process of secondary flux rope formation and coalescence has been shown to occur on a timescale of a few $\omega_{ci}^{-1}$, breaking up a smooth elongated electron current layer into a complex collection of small-scale current sheets (Drake, Swisdak, Schoeffler, et al., 2006; Zhou et al., 2014).

The Magnetospheric Multiscale (MMS) mission offers possibilities for multispacecraft studies of small, ion-scale flux ropes with high spatial and temporal resolution. Ion-scale flux ropes, generated from secondary reconnection, have been reported by Dong et al. (2017). In this paper they observed three active flux ropes located in the reconnection exhaust which grew in size as they moved away from the primary X line. A recent paper by Eastwood et al. (2016) describes a new class of small-scale magnetopause flux ropes. These flux ropes, which had a radius of approximately 500 km or $\sim 7\, d_i$, exhibited filamentary currents and structured non-frozen-in ion motion. The authors conclude that these flux ropes were created by secondary reconnection. Theoretical work has shown that for ion-scale flux ropes, smaller than $<10\, d_i$, ion demagnetization could be a persistent feature (Mandt et al., 1994).

MMS observations of ion-scale, magnetosheath flux ropes have also revealed large difference in particle behavior and wave activity between the core and the edges of flux ropes. The core of the flux rope was characterized by parallel electron beams, electron solitary waves, and electromagnetic lower hybrid drift waves, whereas the edges were characterized by bidirectional electron beams, weak electromagnetic lower hybrid drift waves, whistler waves, and strong broadband electrostatic noise (Huang et al., 2016).

In this paper, we present results from MMS encountering a magnetic structure containing two ion-scale magnetopause flux ropes. The two flux ropes are in direct contact with each other and of similar size. Despite this, the first flux ropes is highly active, whereas the second flux rope is quiescent.

## 2. Methods

### 2.1. Magnetospheric Multiscale Mission

NASA's Magnetospheric Multiscale (MMS) mission was designed to study magnetic reconnection on the electron scale. To achieve this, MMS has been equipped with an instrument suite that offers measurements with a high spatial and temporal resolution, and a satellite separation of <10 km (Burch et al., 2016).

The FIELDS instrument suite, which measures electric and magnetic fields, consists of six sensors: three electric field sensors and three magnetic field sensors (Torbert et al., 2016). Each MMS satellite is equipped with three pairs of double probes: two pairs of spin-plane double probes (SDP) and one pair of axial double probes (SDP). The SDPs are mounted at the end of 60 m long-wire booms and can measure electric fields ranging from DC up to 100 kHz, with a precision of 0.5 mV/m (Lindqvist et al., 2016). The ADP is mounted on two 12.67 m long coilable booms and can measure DC electric fields with a precision of 1 mV/m (Ergun et al., 2016). This allows MMS to directly measure electric fields in 3-D, without having to estimate the axial electric field using the assumption that $\mathbf{E} \cdot \mathbf{B} = 0$. Each MMS satellite is equipped with one analog fluxgate magnetometer (AFG) and one digital fluxgate magnetometer (DFG). The AFG and DFG instruments can measure magnetic fields in the range from DC up to 64 Hz (Russell et al., 2016). The search-coil magnetometer (SCM) has a wider frequency range than AFG and DFG, ranging from 1 Hz up to 6 kHz, allowing it to study whistler waves and kinetic Alfvén waves, which are essential for understanding the physics of the diffusion region (Le Contel et al., 2016).

The Fast Plasma Investigation (FPI) measures electrons and ions with an energy/charge ratio of between 10 eV/$q$ and 30,000 eV/$q$. FPI does not rely on the spacecraft spin to sweep the sky but rather uses multiple instruments, each capable of active field of view control through electrostatic deflection. This allows FPI to achieve full 3-D electron and ion distributions in 30 ms and 150 ms, respectively (Pollock et al., 2016).

### 2.2. Spatio-temporal Difference Method

One method for determining the motion of a constellation of satellites, relative to a magnetic structure, is the Spatio-temporal Difference method (Shi et al., 2006). The Spatio-temporal Difference method assumes that

the magnetic field, **B**, does not exhibit significant temporal variations, $\partial \mathbf{B}/\partial t \approx 0$, and as a consequence the observed variations in the magnetic field are assumed to be due to the motion of the structure relative to the satellites,

$$\frac{d\mathbf{B}}{dt} = -v_{str} \cdot \nabla \mathbf{B}, \quad (1)$$

where $v_{str}$ is the motion of the structure. Since MMS consist of four satellites flying in a tetrahedral formation, $\nabla \mathbf{B}$ can be estimated assuming that the magnetic field exhibits linear variations between the four satellites. In contrast to the often used Discontinuity Analysis method (Haaland et al., 2004; Paschmann & Daly, 2008), the Spatio-temporal Difference method does not require simplifying assumptions about the geometry or motion of the magnetopause such as constant velocity, constant thickness, or constant acceleration and can give velocities in 3-D.

## 3. Observations

The event in question occurred shortly after 03:00:00 UT on 31 December 2016. As can be seen in Figure 1, the position of the MMS constellation was [9.6, −2.8, −0.15] $R_E$ GSE. MMS was on its outbound pass, near the magnetopause and at approximately 11 h magnetic local time. The event was preceded by over 12 h of quiet and stable solar wind conditions with a dynamic pressure of ~2 nPa and low magnetic field clock angle. Similarly, the *Dst* index did not drop below −12 nT in the preceding 12 h period and the *AE* index was typically below 60 nT, both indicating very quiet magnetospheric conditions.

As a first step, we determined the orientation of the magnetopause by using minimum variance of the magnetic field (MVAB) under the constraint that $\langle B_N \rangle = 0$ (Paschmann & Daly, 1998). In MVAB the minimum variance component corresponds to the normal of the magnetopause, whereas the intermediate and maximum variance components are tangential to the magnetopause. The results of the MVAB analysis can be found in Table 1. In addition, the orientation of each flux rope was determined using minimum directional derivative (MDD) analysis of the magnetic field (Shi et al., 2005). In MDD, the minimum derivative direction corresponds to the principal (invariant) axis of a flux rope. As can be seen in Table 2, the ratio between intermediate and minimum eigenvalues are 10 and 916 for the first and second flux ropes, respectively. This shows that both flux ropes have a well-defined invariant direction. The principal axis of both flux ropes are closely aligned with the *M* direction of MVAB analysis, offset by 5 and 9°, respectively. Lastly, we performed a maximum variance of current (MVAJ) analysis, with the current calculated from FPI particle moments data. The MVAJ component of maximum variance, corresponding to the direction of the magnetopause current sheet, was less than 10° from the MVAB intermediate direction. This indicates that the results from the MVAB and MDD analysis are robust. From here on, vector quantities are given using the NML coordinate system from the MVAB analysis, where *N* is $\approx +\mathrm{GSE}_X$ and *M* and *L* lie in the $\mathrm{GSE}_Y$-$\mathrm{GSE}_Z$ plane, rotated by approximately 45°, with *M* pointing toward $+\mathrm{GSE}_Y$.

As can be seen in Figure 2a, the polarity, negative-positive, of the two sequential, asymmetric, bipolar $B_N$ signatures indicates that MMS entered the flux ropes from the south, that is, the flux ropes are moving south relative to MMS. Figure 2c shows that $B_L$ goes from positive to negative, indicating that MMS is moving toward the magnetosheath. This is in agreement with the observed ion velocities, Figures 2f–2h, which indicate that the flux ropes are moving southward and earthward. As can be seen in Figure 2b the event exhibits a strong guide field of approximately 40 nT, equivalent to a normalized guide field of 0.85.

As can be seen in Figure 2i, the motion estimated using the Spatio-temporal Difference method predicts that the magnetic structure containing the two flux ropes is moving southward and earthward, corresponding to MMS moving northward and toward the magnetosheath. It is worth noting that while there is a qualitative agreement between the velocities from the Spatio-temporal Difference method and the ion bulk velocity, the ions are generally moving faster than the magnetic structure.

Figure 2j shows the formation of the four MMS satellites, at 03:00:00 UT, described in our *NML* coordinate system. At this time, the average spacecraft separation is 13 km, with the minimum separation between MMS 1 and MMS 4 (7 km) and the maximum separation between MMS 2 and MMS 3 (15 km). As can be inferred from Figures 2a–2c, MMS 4 is the first satellite to enter the flux rope, with MMS 1 closely behind, followed by MMS 3, and finally MMS 2. This is what one would expect from the combination of the observed flux rope motion and satellite formation. The average time separation between first and last satellites, MMS 4 and MMS 2 respectively, is <0.5 s.

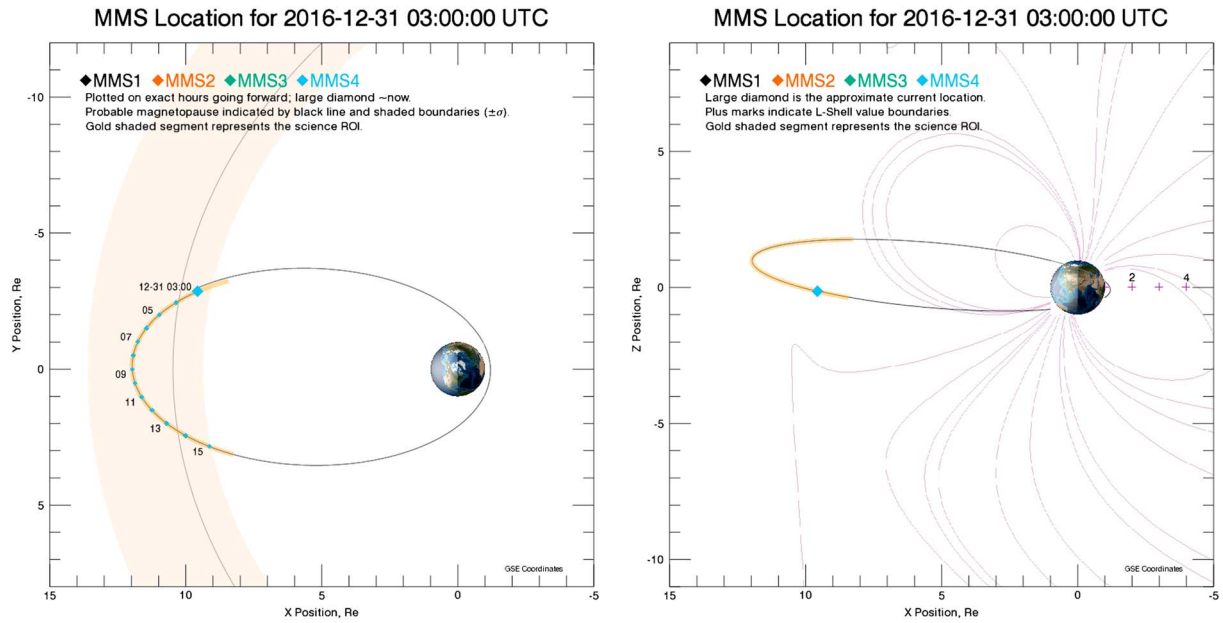


**Figure 1.** Position of MMS constellation at 03:00:00 UT.

As can be inferred from the dashed lines in Figure 2i, the first flux rope has an *N* direction half width, measured from the magnetospheric edge to the magnetopause, of 48 km or 1.6 magnetosheath ion skin depths ($d_i$). The second flux rope has a half width, measured from the magnetopause to the magnetosheath edge, of 52 km (1.7 $d_i$). These numbers are somewhat conservative as we do not cross through the center of either flux rope, where they would have their largest extent in the *N* direction.

The first flux rope has an *L* direction half width, measured from the $B_N$ reversal at the center of the flux rope to the in-plane null between the two flux ropes, of 37 km (1.2 $d_i$). This is comparable to the distance from where MMS enters the first flux rope to the center of the flux rope, 28 km (0.9 $d_i$). The corresponding half width of the second flux rope is 53 km (1.8 $d_i$), and the distance from the center of the flux rope to where MMS exits the flux rope is 81 km (2.7 $d_i$). Based on the above, we can estimate that the two flux ropes have a size of approximately $4 \times 2.5\ d_i$ and $4 \times 4.5\ d_i$, respectively.

We will use the observations from MMS 4 to illustrate the overall features of the two flux ropes. As can be seen in Figure 3b, prior to MMS 4 entering the first flux rope, $v_{str,L}$ is close to zero. Starting at approximately 03:00:11.7 UT, $v_{str,L}$ becomes increasingly negative. The minimum velocity of −46 km/s is reached at around 03:00:19 UT, just prior to MMS 4 exiting the second flux rope. From here on, the structure slows down but keeps moving southward for the remainder of the time interval. Throughout this time interval, $v_{str,N}$ is negative indicating that both flux ropes are moving toward the magnetosphere, which is consistent with the large-scale variations seen in $B_L$. This shows that the increase and subsequent decrease in $B_L$ seen between 03:00:12 UT and 03:00:15 UT is not due to magnetopause moving back and forth across the satellites but due to the internal structure of the flux ropes.

Figure 3c shows the electric current, which is calculated from FPI particle moments. Around 03:00:13 UT, as MMS 4 enters the first flux rope, we observe enhanced currents, with a maximum of $\sim 2,500\ \mathrm{nA/m^2}$. Inside the first flux rope, we observe a broad region of strong currents, with a maximum value of $\sim 2,200\ \mathrm{nA/m^2}$ occurring at approximately 03:00:14.5 UT. This coincides with MMS 4 passing the center of the first flux rope, indicated by the reversal in $B_N$. Around 03:00:16 UT, at the interface between the two flux ropes, a small spike of $\sim 1,000\ \mathrm{nA/m^2}$ is observed. The second flux rope exhibits a broad current feature, reaching a peak value of $730\ \mathrm{nA/m^2}$ around 03:00:17 UT. This coincides with the center of the second flux rope, inferred from the $B_N$ reversal. At 03:00:19.3 UT, as MMS 4 exits the second flux rope, a narrow spike with a peak value of $\sim 1,200\ \mathrm{nA/m^2}$ is observed. It should be noted that in both flux ropes the perpendicular current is comparable to, and in several places

**Table 1**
*Vector Basis of NML Coordinate System Derived From MVAB*

| | *N* | *M* | *L* |
|---|---|---|---|
| $GSE_X$ | 0.953 | −0.246 | −0.176 |
| $GSE_Y$ | 0.298 | 0.666 | 0.685 |
| $GSE_Z$ | −0.051 | −0.704 | 0.708 |

**Table 2**
*Orientation of Flux Ropes Derived From MDD*

| | Flux rope 1 | | | Flux rope 2 | | |
|---|---|---|---|---|---|---|
| | Maximum | Intermediate | Minimum | Maximum | Intermediate | Minimum |
| $GSE_X$ | 0.948 | −0.070 | −0.311 | 0.973 | −0.006 | −0.230 |
| $GSE_Y$ | −0.253 | −0.756 | −0.601 | −0.186 | −0.605 | −0.590 |
| $GSE_Z$ | −0.193 | 0.651 | −0.734 | −0.134 | 0.797 | −0.775 |
| $\langle\lambda\rangle$ | 0.150 | 0.020 | 0.002 | 0.143 | 0.012 | 1.31e−5 |

larger than, the parallel current. This means that $\mathbf{J} \times \mathbf{B} \neq 0$ and that neither flux rope can be considered force free. By comparing the current with the electron velocity, Figure 3g, and the ion velocity, Figure 3i, it is clear that the variations in the current are dominated by electron dynamics.

As can be seen in Figure 3e, MMS 4 initially observes counterstreaming low-energy electrons, with the lowest fluxes around 90° pitch angle, indicative of magnetospheric electrons on closed field lines. Between 03:00:12 UT and 03:00:13 UT, we observe an enhancement of both low- and middle-energy electrons for pitch angles 135°, indicating an active X line north of MMS. Around 03:00:13 UT, as MMS 4 enters the first flux rope, we can observe a brief field-aligned beam, immediately followed by a brief anti-field-aligned beam.

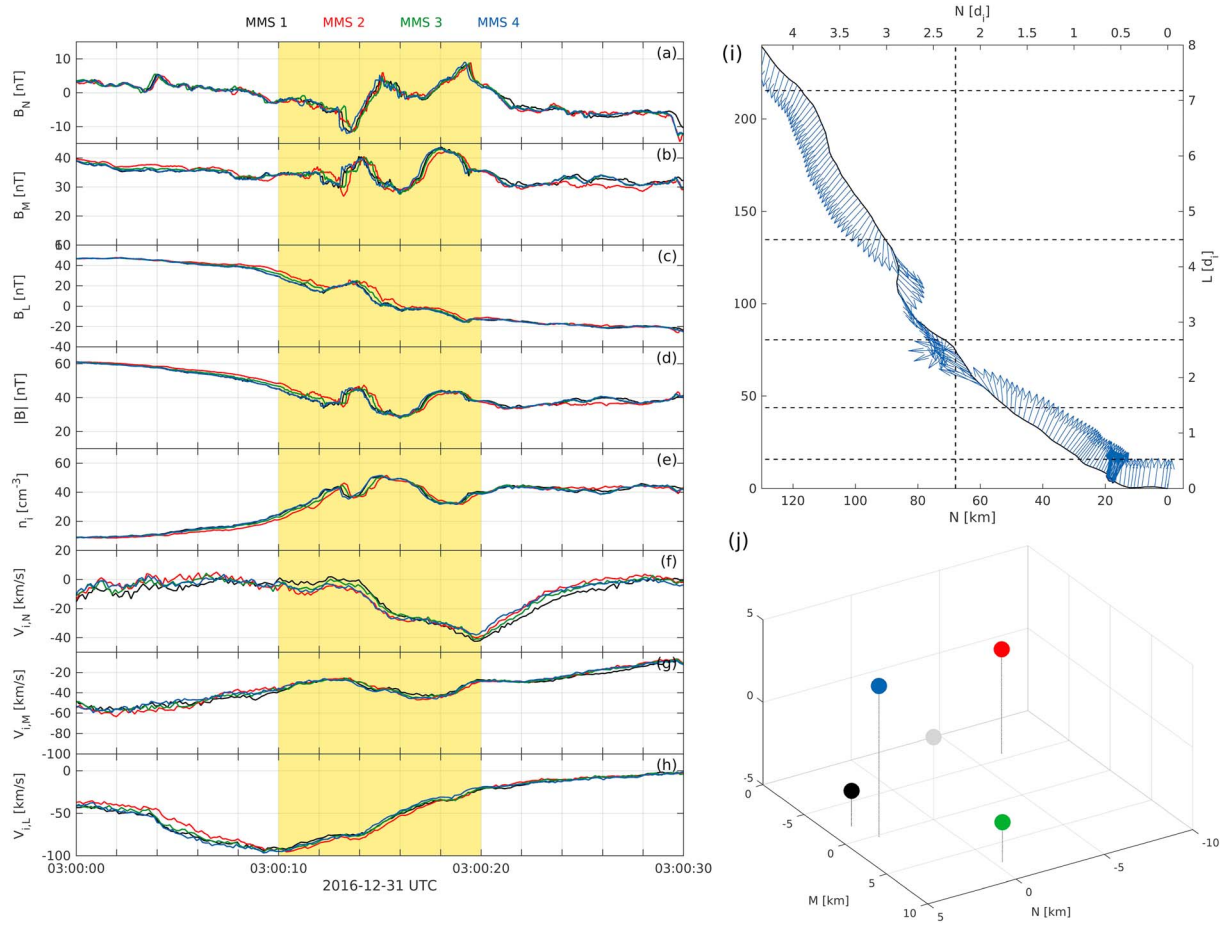


**Figure 2.** Comparison of the event as seen by MMS 1 to MMS 4. (a) Normal magnetic field $B_N$; (b) tangential (dawn/dusk) magnetic field $B_M$; (c) tangential (north/south) magnetic field $B_L$; (d) magnetic field strength $|B|$; (e) ion density $n_i$; (f) ion bulk velocity $V_{i,N}$; (g) ion bulk velocity $V_{i,M}$; (h) ion bulk velocity $V_{i,L}$; (i) path of the MMS constellation between 03:00:10 UT and 03:00:20 UT, the feather plot represents the unit vector of the magnetic field averaged over the tetrahedron; and (j) MMS formation at 03:00:00 UT in boundary-normal coordinates. The dashed vertical line indicates the location of the magnetopause. Starting from the bottom; the dashed horizontal lines indicate MMS entering first flux rope, center of first flux rope, interface between first and second flux rope, center of second flux rope, and MMS exiting the second flux rope.

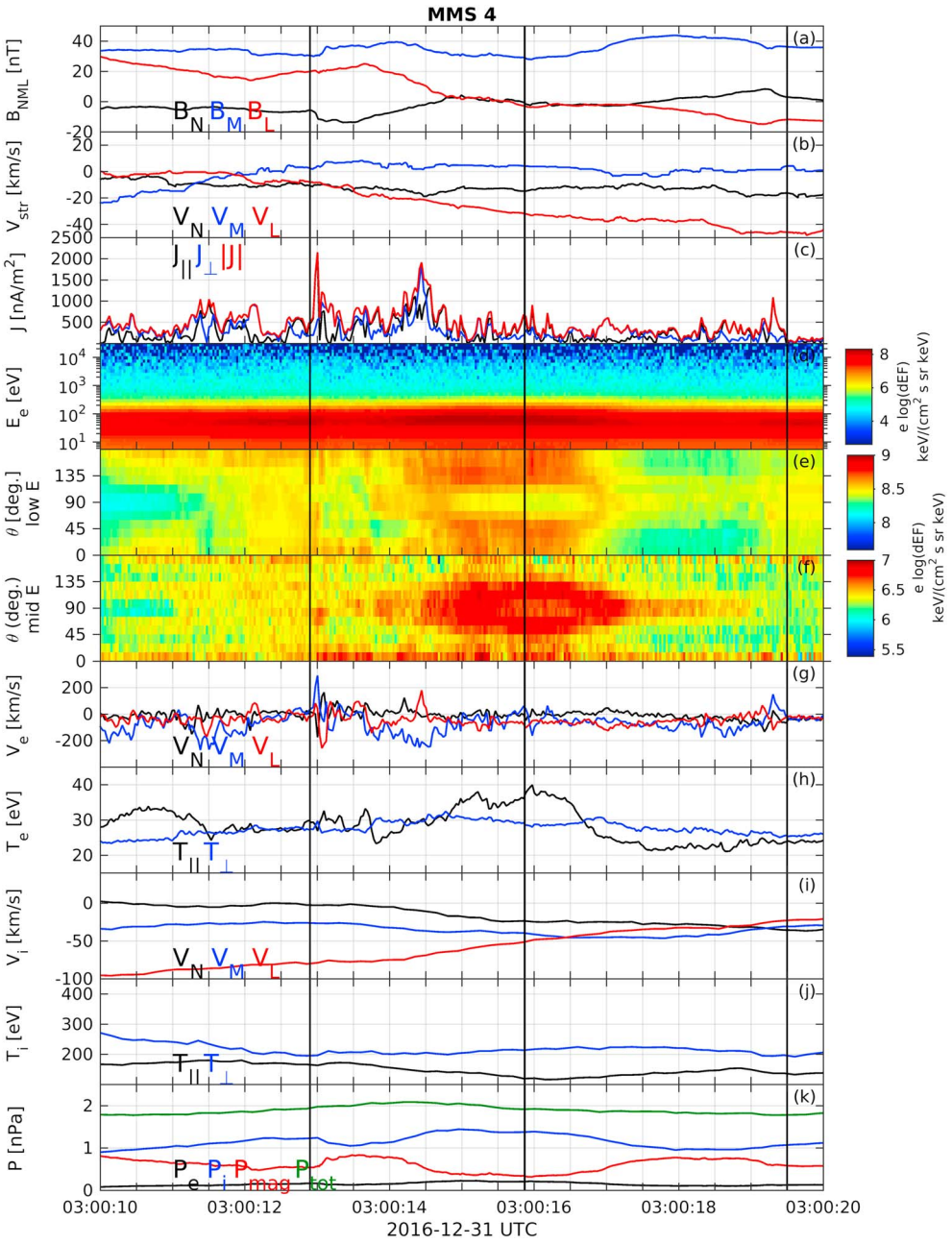


**Figure 3.** Summary of the two flux ropes, as observed by MMS 4. (a) Magnetic field; (b) velocity of the flux rope; (c) currents: parallel (black), perpendicular (blue), and total (red); (d) electron energy spectrogram; (e) pitch angle spectrogram 0–200 eV electrons; (f) pitch angel spectrogram for 200–2,000 eV electrons; (g) electron velocity; (h) electron temperature; (i) ion velocity; (j) ion temperature; and (k) pressure. The vertical black lines indicate the extent of the two flux ropes.

Between 03:00:13 UT and 03:00:14.7 UT the low-energy electrons exhibit bursts of counterstreaming electrons, whereas the middle-energy electrons exhibit enhanced field-aligned fluxes. Between 03:00:14.7 UT and 03:00:16.5 UT, centered around the interface between the two flux ropes, the counterstreaming electrons become a strong and persistent feature. Starting at 03:00:16.5 UT, the electrons are gradually focused toward 90° pitch angle. In contrast, the middle-energy electrons (200–2,000 eV), Figure 3f, exhibit a trapped population during this time period. From 03:00:16.5 UT to 03:00:19.3 UT the 45°–135° pitch angle electrons exhibit enhanced fluxes, after which the electrons become nearly isotropic. Throughout this time interval

the ions show a clear enhancement at pitch angles >90° for all energies. This corresponds to a southward and dawnward bulk flow seen in Figures 2f–2h.

As can be seen in Figure 3h, the interface between the two flux ropes exhibits significant parallel electron heating. In contrast, the ions mainly exhibit a gradual decrease in temperature as MMS moves toward the magnetosheath.

As can be seen in Figure 3k, the pressure balance is dominated by the magnetic and ion pressures, with the electrons playing only a minor role. There is a slight, ∼10%, increase in the total pressure seen between the edges of the first flux rope and the center of the first flux rope. It is worth pointing out that neither MMS 4 nor the other satellites passes through the center of the first flux rope. Therefore, the maximum pressure we observe is likely to be lower than the actual maximum pressure. Inside the second flux rope the total pressure is relatively constant due to the anticorrelation between the ion pressure and magnetic pressure terms.

Figures 4b–4d compare the electric field measured by EDP and the electron and ion convection electric fields $-\mathbf{v_e} \times \mathbf{B}$ and $-\mathbf{v_i} \times \mathbf{B}$. From the good agreement between $\mathbf{E}_{\mathrm{EDP}}$ and $-\mathbf{v_e} \times \mathbf{B}$, we can draw the conclusion that the electrons are frozen-in. However, this is not the case for the ions. This is especially clear in Figure 4b, where between 03:00:10 UT and 03:00:16 UT there is a clear offset between $\mathbf{E}_{\mathrm{EDP}}$ and $-\mathbf{v_i} \times \mathbf{B}$. This indicates that MMS has entered an ion diffusion region. Around 03:00:13 UT, at the start of the first flux rope, all components of the electric field exhibit low-frequency wave activity, most noticeably in $E_M$ and $E_L$. At 03:00:14.4 UT, we can observe a ∼10 mV/m spike in $E_N$ and $-\mathbf{v_e} \times \mathbf{B}$. Between 03:00:15.8 UT and 03:00:16 UT, EDP observes a region of rapidly fluctuating electric fields with a magnitude of a few mV/m. These signatures are especially pronounced in $E_M$, which is closely aligned with the magnetic field. In contrast, the second flux rope exhibits a weak, quiet electric field with few notable internal features.

The electric and magnetic spectral power densities, seen in Figures 4e–4g, exhibit a number of different types of wave modes. The strong electric fields observed upon entering the first flux rope are low-frequency, broadband, starting below 10 Hz and extending up to approximately 400 Hz. This electric field structures is in turn flanked by broadband electrostatic emissions which have their maximum intensity around 1 kHz, close to the electron cyclotron frequency ($f_{\mathrm{ce}}$). These broadband, electrostatic waves consist of a series of bipolar, mostly parallel electric field perturbations (not shown), indicative of solitary structures. These bursts of broadband activity are observed in both flux ropes but are the most prominent around 03:00:13 UT, when MMS 4 enters the first flux rope. In contrast, the second flux rope exhibits weaker broadband signatures but distributed over a large number of ∼100 ms bursts.

Between 03:00:15 UT and 03:00:16.5 UT, MMS 4 observes narrowband, right-hand polarized, electromagnetic waves, exhibiting a significant parallel electric field. Initially, the frequency is approximately 400 Hz, decreasing to a frequency of approximately 200 Hz over the course of ∼ 1 s. This is followed by a 0.5 s period where the frequency is stable around 200 Hz. During this time period the electromagnetic wave activity exhibits fine-scale structure with short burst on the order of 100 ms. This fine-scale structure is especially pronounced in the parallel electric field.

Figure 4h shows that around 03:00:13 UT, all the three components of the current exhibit large, rapid fluctuations. $J_N$ exhibits a bipolar signature of $\sim 1,100\ \mathrm{nA/m^2}$, $J_M$ a negative spike of $\sim 2,200\ \mathrm{nA/m^2}$, and $J_L$ a bipolar signature with a magnitude of $\sim 1,000\ \mathrm{nA/m^2}$. Between 03:00:13.5 UT and 03:00:15 UT we can observe an extended region with positive $J_M$. The maximum current of $\sim 1,700\ \mathrm{nA/m^2}$ occurs around 03:00:14.5 UT, coinciding with a negative peak in $J_L$ of approximately $2,000\ \mathrm{nA/m^2}$. This is where we observe the reversal in $B_N$, indicating that MMS 4 was close to the center of the flux rope, in terms of the position in the $L$ direction. Between the two flux ropes there are two current sheets with $J_M$ of approximately $-600\ \mathrm{nA/m^2}$ separated by a sheet of positive $J_M$ of similar magnitude. In the second flux rope, the currents are generally much weaker but we can observe an extended region with positive $J_M$. The peak value of $\sim 600\ \mathrm{nA/m^2}$ occurs at approximately 03:00:18.7 UT, close to where we observe a $B_N$ reversal. At 03:00:19.3 UT, as MMS 4 exits the second flux rope we observe bipolar signatures similar to those seen upon entering the first flux rope. However, the magnitude of these current spikes is considerably smaller, $\sim 600\ \mathrm{nA/m^2}$.

As can be seen in Figure 4i, the spike in the current and electric field which is observed at 03:00:13 UT is associated with significant electron frame energy dissipation ($\mathbf{J} \cdot \mathbf{E}'$) (Zenitani et al., 2011). At this time $\mathbf{J} \cdot \mathbf{E}'$ is positive and approximately $5\ \mathrm{nW/m^3}$. This shows that the electrons are being energized. In contrast, around 03:00:14.4 UT, near the center of the first flux rope, $\mathbf{J} \cdot \mathbf{E}'$ peaks at $-2.5\ \mathrm{nW/m^3}$, indicating

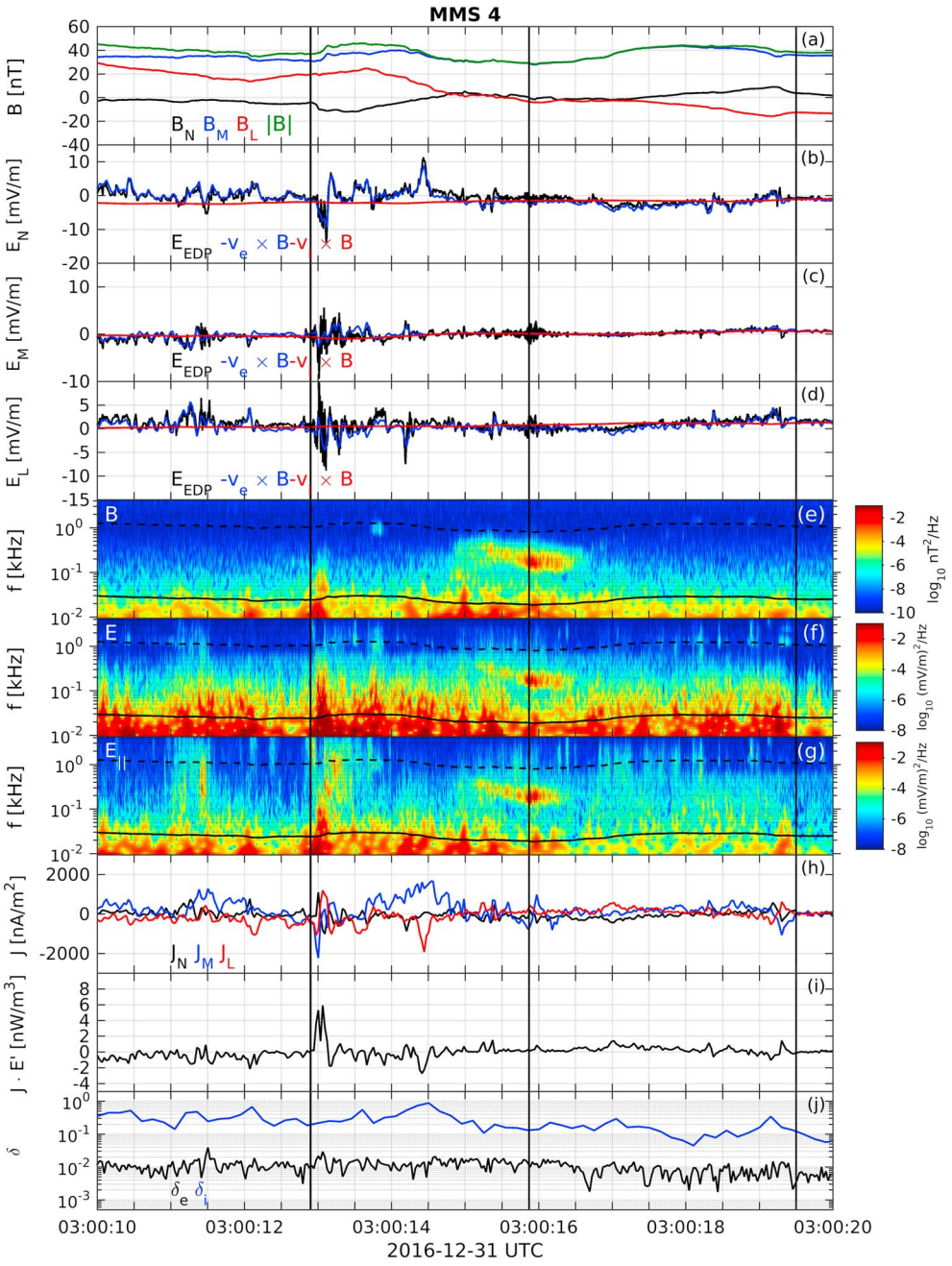


**Figure 4.** Comparison of particle moments and electric field from MMS 4. (a) Magnetic field in boundary-normal coordinates; (b) normal electric field from EDP (black), $-\mathbf{v_e} \times \mathbf{B}$ (blue), and $-\mathbf{v_i} \times \mathbf{B}$ (red); (c) tangential (dawn/dusk) electric field from EDP (black), $-\mathbf{v_e} \times \mathbf{B}$ (blue), and $-\mathbf{v_i} \times \mathbf{B}$ (red); (d) tangential (north/south) electric field from EDP (black), $-\mathbf{v_e} \times \mathbf{B}$ (blue), and $-\mathbf{v_i} \times \mathbf{B}$ (red); (e) power spectral density of the magnetic field; (f) power spectral density of the electric field; (g) power spectral density of the parallel electric field; (h) electric current; (i) energy conversion; and (j) Lorentz ratio ($\delta$). The vertical black lines indicate the extent of the two flux ropes. The solid black lines in Figures 4e–4g represent the lower hybrid frequency and the dashed black lines the electron cyclotron frequency.

a generator region. Around 03:00:15.8 UT, at the interface between the two flux ropes, $\mathbf{J} \cdot \mathbf{E}'$ is positive but never exceeds 2 nW/m$^3$. As one may predict from the previous figures, the second flux rope does not exhibit a significant energy conversion. Between 03:00:16 UT and 03:00:18 UT, $\mathbf{J} \cdot \mathbf{E}'$ is positive but <2 nW/m$^3$. The second flux rope exhibits two bipolar structures of approximately ±1 nW/m$^3$ around 03:00:18.3 UT and 03:00:19.3 UT.

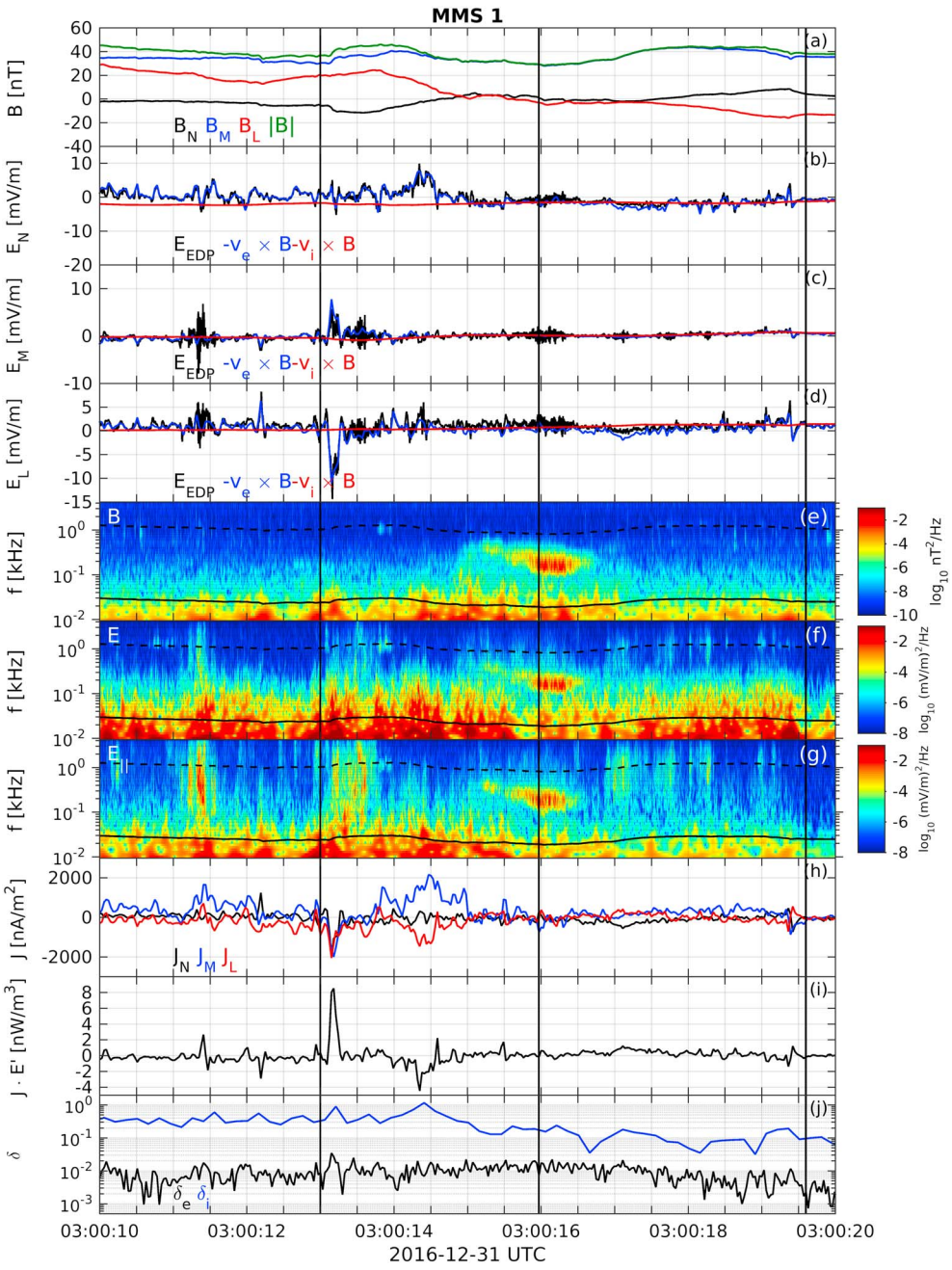


**Figure 5.** Comparison of particle moments and electric field from MMS 1. (a) Magnetic field in boundary-normal coordinates; (b) normal electric field from EDP (black), $-\mathbf{v_e} \times \mathbf{B}$ (blue), and $-\mathbf{v_i} \times \mathbf{B}$ (red); (c) tangential (dawn/dusk) electric field from EDP (black), $-\mathbf{v_e} \times \mathbf{B}$ (blue), and $-\mathbf{v_i} \times \mathbf{B}$ (red); (d) tangential (north/south) electric field from EDP (black), $-\mathbf{v_e} \times \mathbf{B}$ (blue), and $-\mathbf{v_i} \times \mathbf{B}$ (red); (e) power spectral density of the magnetic field; (f) power spectral density of the electric field; (g) power spectral density of the parallel electric field; (h) electric current; (i) energy conversion; and (j) Lorentz ratio ($\delta$). The vertical black lines indicate the extent of the two flux ropes. The solid black lines in Figures 5e–5g represent the lower hybrid frequency and the dashed black lines the electron cyclotron frequency.

Figure 4j shows the Lorentz ratio ($\delta$) for the electrons and ions, which is the ratio between the electric and magnetic forces experienced by a particle in its rest frame, which serves as an estimate of the degree of particle demagnetization. The Lorentz ratio is defined as $\delta = |\mathbf{E} + \mathbf{v} \times \mathbf{B}| / (w_\perp B)$, where $\mathbf{v}$ is the bulk velocity of the particle species and $w_\perp$ is the thermal speed of the particle species (Scudder et al., 2008). Throughout the entire time interval, $\delta_e$ is on the order of 0.01 which indicates that the electrons are fully magnetized. Just prior to MMS 4 entering the first flux rope $\delta_i$ is around 0.1. Starting at 03:00:04 UT until 03:00:16 UT, $\langle \delta_i \rangle$ is 0.33

with several spikes in excess of 0.8. This suggests that we are observing an ion diffusion region. Around 03:00:17 UT, shortly after MMS 4 enters the second flux rope, $\delta_i$ decrease and is typically $< 0.2$ for the remainder of the event, indicating that in the second flux rope the ions are mostly magnetized.

Next we turn our attention to MMS 1, Figure 5, which at this point is located approximately 7 km from MMS 4, mostly southward of MMS 4, and trailing by approximately 0.1 s. Just as was the case for MMS 4, MMS 1 observes enhanced electric fields starting around 03:00:13 UT, right as it enters the first flux rope. Where MMS 4 saw oscillations of similar magnitude in all three components, MMS 1 observes a single positive excursion in $E_M$, with a peak value of $\sim$ 5.5 mV/m, and a single negative excursion in $E_L$, with a peak magnitude of 14 mV/m. Superimposed on these two peaks is some low-amplitude, low-frequency wave activity.

When comparing with the electric power spectral density plot, Figures 5f and 5g, one can see that the broadband, low-frequency activity is most pronounced below 200 Hz, as opposed to MMS 4 which observed pronounced activity up to 400 Hz. The broadband $\sim$ 1 kHz solitary waves exhibit the same large-scale features but are generally stronger and covers a wider frequency range than was the case for MMS 4. The interface between the two flux ropes exhibits similar electromagnetic wave signatures, with one region exhibiting a gradually decrease in frequency from 400 Hz to 200 Hz, followed by a region with a near constant frequency around 200 Hz.

Around 03:00:13.3 UT, upon entering the first flux rope, MMS 1 observes three monopolar, $\sim$2000 nA/m$^2$, negative excursions in all current components. Between 03:00:13.7 UT and 03:00:15 UT, MMS 1 observes the main, axial, $J_M$ current sheet of the first flux rope flux. Here the peak current is $\sim$2, 200 nA/m$^2$, somewhat higher than observed by MMS 4 but exhibiting the same overall large-scale structure. In the same time period we can observe a broad negative excursion in $J_L$ with peak magnitude of $\sim$1500 nA/m$^2$. Compared to when the same $J_L$ structure was observed by MMS 4, the current sheet is wider and weaker. At 03:00:16 UT, right as MMS 1 encounters the second flux rope, we observe a single negative spike in $J_M$ of $-$750 nA/m$^2$. At 03:00:19.4 UT, as MMS 1 leaves the second flux rope, we observe bipolar variations in all components of the current, with a magnitude of 500$-$800 nA/m$^2$. In $J_N$ and $J_M$ the bipolar structures are negative-positive, whereas in $J_L$ the variation is positive-negative.

MMS 1 observes the same type of pattern in the energy conversion as MMS 4, but in general, the magnitudes are larger. Around 03:00:13 UT the peak energy conversion is $\sim$8.5 nW/m$^3$ and at the center of the first flux rope the energy conversion peaks at approximately $-$4.5 nW/m$^3$.

As seen in Figure 5j, just like in MMS 4 the first flux rope shows a larger degree of ion demagnetization than the second flux rope. At 03:00:14.4 UT, $\delta_i > 1$ indicating that the ions are completely demagnetized (Maynard et al., 2012).

The next satellite to encounter the flux ropes is MMS 3, summarized in Figure 6. As MMS 3 enters the flux rope, the electric field exhibits a resolved, asymmetric, bipolar signature in all three components. The normal component, $E_N$, changes from +6.5 to $-$2.5 mV/m and $E_M$ from +10 to $-$5 mV/m. In contrast, $E_L$ exhibits a bipolar signature with the opposite polarity, going from $-$15 mV/m to +7 mV/m. Around 03:00:14.7 UT, near the center of the first flux rope, MMS 3 observes a 7 mV/m spike in $E_L$. For the remainder of the event, MMS 3 does not observe any strong electric fields. The power spectral density plots, Figures 6e$-$6g, exhibit only minor differences from those of MMS 1. The most notable difference is that the electric fields observed around 03:00:13 UT exhibit a somewhat lower frequency.

Upon entering the first flux rope, MMS 3 observes a resolved negative-positive bipolar signature in $J_N$, going from $-3,000$ nA/m$^2$ to $\sim$1, 200 nA/m$^2$. $J_M$ and $J_L$ both exhibit negative spikes with a magnitudes of $\sim$1, 900 nA/m$^2$ and $\sim$2, 600 nA/m$^2$, respectively. This is similar to what was observed by MMS 1, but the magnitude is approximately 25% larger. It is worth noting that while MMS 4 did observe a similar bipolar signature in $J_N$, it had the opposite polarity and roughly half of the amplitude. The main $J_M$ current sheet exhibits a similar maximum of $\sim$2, 100 nA/m$^2$. However, we now observe three $J_M$ current sheets, separated by deep local minima of $\sim$350 nA/m$^2$. Between 03:00:15 UT and 03:00:16 UT, MMS 3 observes two extended regions with negative $J_M$, separated by a brief positive spike.

The energy conversion is dominated by a strong peak occurring at 03:00:13.4 UT, just as MMS 3 enters the first flux rope. The peak energy conversion is $\sim$9.5 nW/m$^3$. Between 03:00:14 UT and 03:00:14.8 UT, we can observe an extended region of low, negative $\mathbf{J} \cdot \mathbf{E}'$. Both these regions exhibit $\delta_i > 1$, indicating that the ions are fully demagnetized (Maynard et al., 2012).

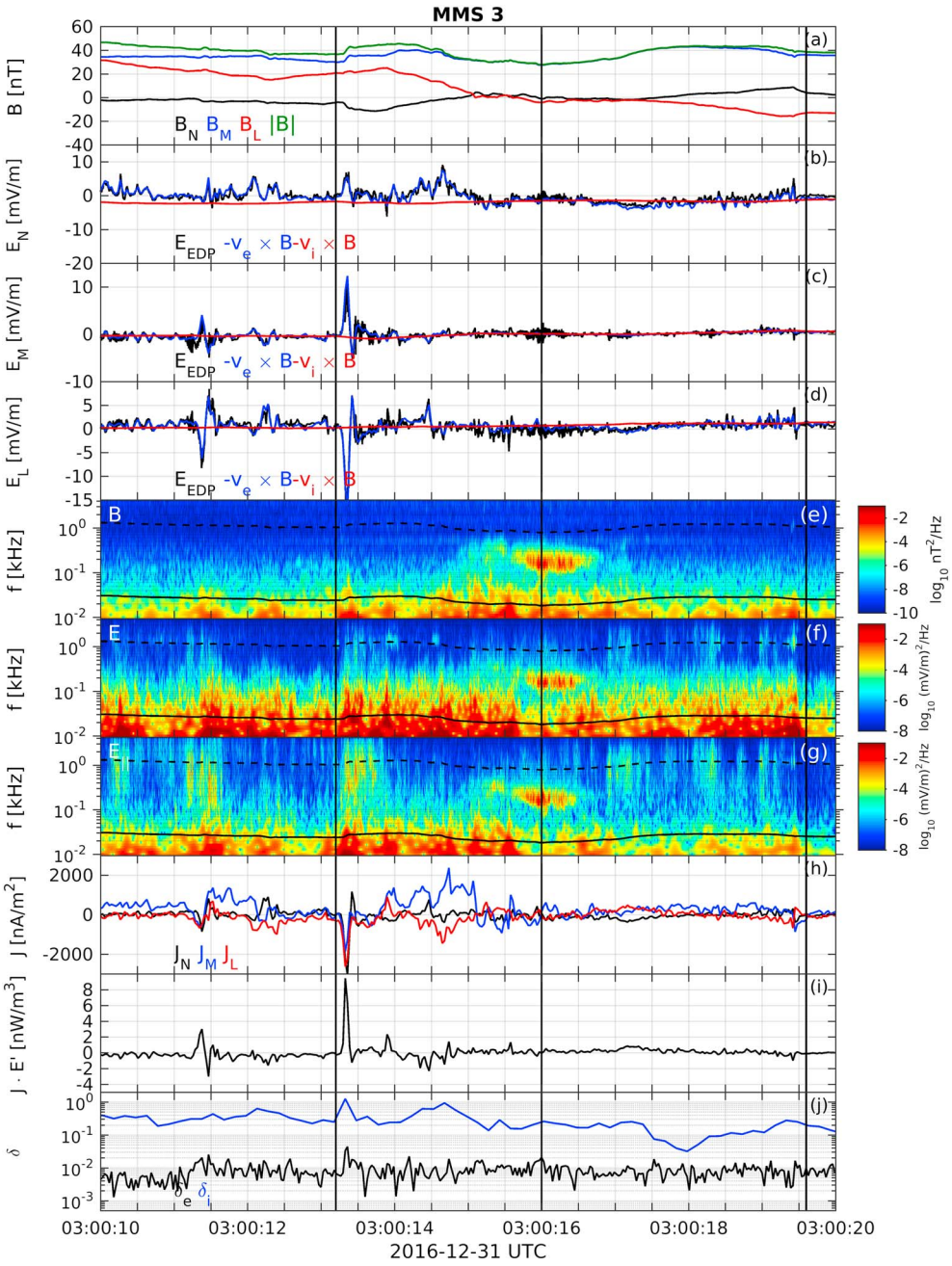


**Figure 6.** Comparison of particle moments and electric field from MMS 3. (a) Magnetic field in boundary-normal coordinates; (b) normal electric field from EDP (black), $-\mathbf{v_e} \times \mathbf{B}$ (blue), and $-\mathbf{v_i} \times \mathbf{B}$ (red); (c) tangential (dawn/dusk) electric field from EDP (black), $-\mathbf{v_e} \times \mathbf{B}$ (blue), and $-\mathbf{v_i} \times \mathbf{B}$ (red); (d) tangential (north/south) electric field from EDP (black), $-\mathbf{v_e} \times \mathbf{B}$ (blue), and $-\mathbf{v_i} \times \mathbf{B}$ (red); (e) power spectral density of the magnetic field; (f) power spectral density of the electric field; (g) power spectral density of the parallel electric field; (h) electric current; (i) energy conversion; and (j) Lorentz ratio ($\delta$). The vertical black lines indicate the extent of the two flux ropes. The solid black lines in Figures 6e–6g represent the lower hybrid frequency and the dashed black lines the electron cyclotron frequency.

The last satellite to enter the flux ropes is MMS 2, shown in Figure 7. As can be seen in Figure 7a, MMS 2 does not observe the same magnetic field signatures as the other MMS satellites. Whereas the other satellites observe a distinct decrease in $B_N$ and an increase in $|\mathbf{B}|$ as they enter the first flux rope, MMS 2 observes a more gradual transition. In addition, MMS 2 observes a number of small spikes in $B_L$ not observed by the other satellites.

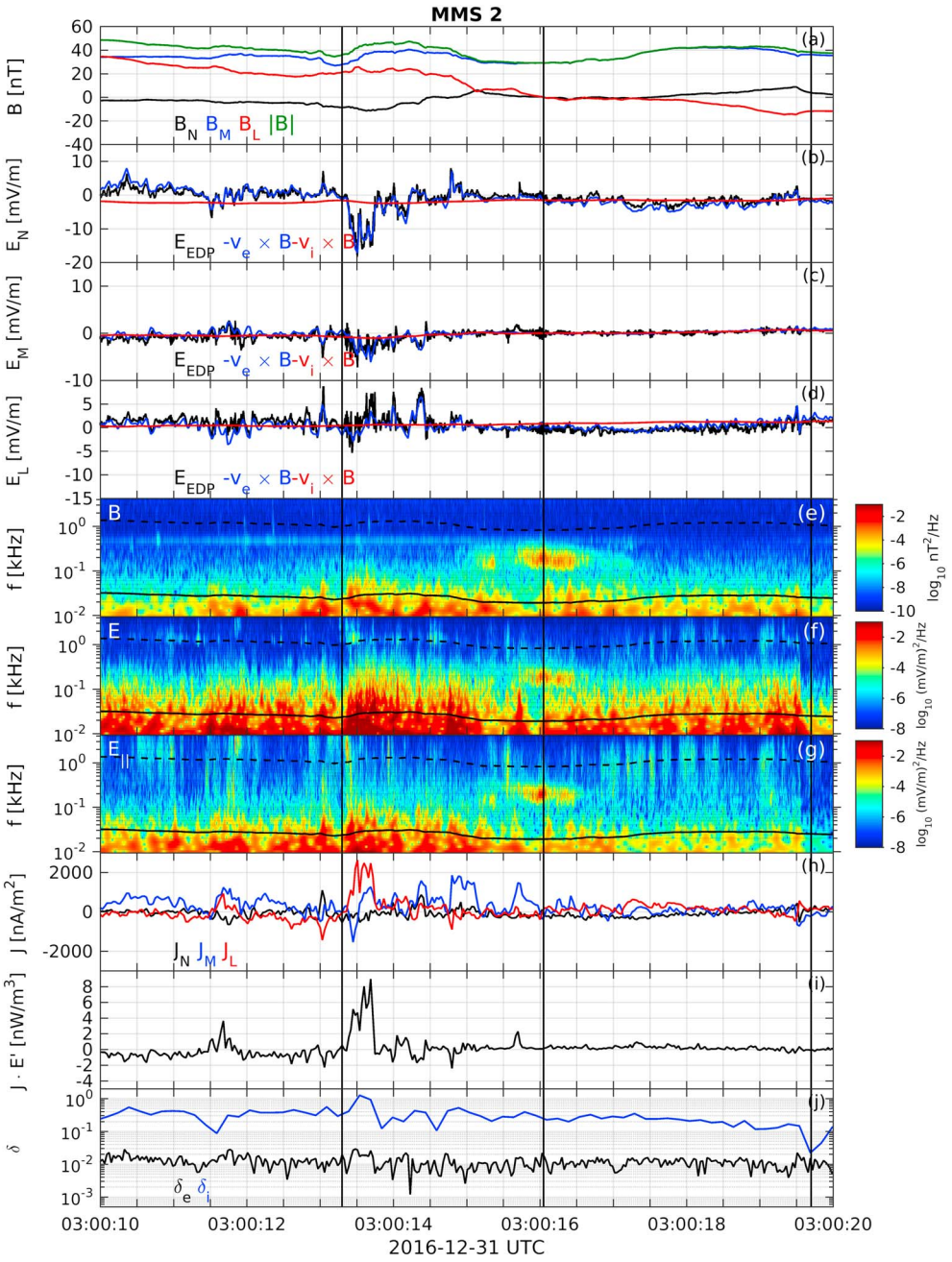


**Figure 7.** Comparison of particle moments and electric field from MMS 2. (a) Magnetic field in boundary-normal coordinates; (b) normal electric field from EDP (black), $-\mathbf{v_e} \times \mathbf{B}$ (blue), and $-\mathbf{v_i} \times \mathbf{B}$ (red); (c) tangential (dawn/dusk) electric field from EDP (black), $-\mathbf{v_e} \times \mathbf{B}$ (blue), and $-\mathbf{v_i} \times \mathbf{B}$ (red); (d) tangential (north/south) electric field from EDP (black), $-\mathbf{v_e} \times \mathbf{B}$ (blue), and $-\mathbf{v_i} \times \mathbf{B}$ (red); (e) power spectral density of the magnetic field; (f) power spectral density of the electric field; (g) power spectral density of the parallel electric field; (h) electric current; (i) energy conversion; and (j) Lorentz ratio ($\delta$). The vertical black lines indicate the extent of the two flux ropes. The solid black lines in Figures 7e–7g represent the lower hybrid frequency and the dashed black lines the electron cyclotron frequency.

As can be seen in Figure 7b, upon entering the first flux rope, MMS 2 observes an extended region with large $E_N$, with a peak value of approximately −17 mV/m. At the same time $E_M$ and $E_L$, Figures 7c and 7d, exhibit rapid fluctuations with an amplitude of approximately 5 mV/m. In contrast to the other satellites, MMS 2 observes several regions with enhanced electric fields inside the first flux rope, most notably in the $E_N$ and $E_L$ components.

The power spectral density plots found in Figures 7e–7g further highlight the differences between MMS 2 and the other satellites. In contrast to the other satellites, MMS 2 observes little wave activity at the edge of the first flux rope and mostly below the lower hybrid frequency (indicated by the solid black line). Inside the first flux rope, MMS 2 observes an extended region, ~2 s of mostly perpendicular electric fields with a frequency just above the lower hybrid frequency. There are a few bursts of electrostatic wave activity but fewer and less intense than observed by the previous satellites. The interface between the two flux ropes still exhibits electromagnetic wave activity but over a shorter time period and at a constant frequency of approximately 200 Hz. The second flux rope is still characterized by short bursts of broadband electrostatic waves, exhibiting the peak intensity around the electron cyclotron frequency.

As can be seen in Figure 7h, the currents observed by MMS 2 have little resemblance to those of the other satellites. The most striking feature is observed at 03:00:13.3 UT, when MMS 2 enters the first flux rope. Where the other satellites observe narrow spikes in all components, MMS 2 is dominated by a broad $J_L$ current sheet, with a peak value exceeding ~2, 500 nA/m$^2$. This region is associated with significant electron energization, where $\mathbf{J} \cdot \mathbf{E}'$ exceeds 8 nW/m$^3$. Inside the first flux rope, MMS 2 observes three $J_M$ current sheets separated by $J_M$ current reversal. The second flux rope exhibits the same over all characteristics as seen by the other satellites, with low currents and few distinguish features apart from a bipolar signature at the trailing edge of the flux rope.

## 4. Discussion

In addition to our original interpretation, two sequential flux ropes, the two bipolar $B_N$ signatures could arise from MMS sampling the same flux rope at two different times or by a single flux rope immersed in a corrugated magnetopause. The first case could occur as the result of the magnetopause flapping past MMS. However, the ion bulk velocity as well as the velocity determined through the Spatio-temporal Difference method indicates that the magnetic structure has a steady southward and earthward motion during the time period in question.

Instead of a second flux rope, the second bipolar $B_N$ signature could arise from a corrugated magnetopause. The second, weaker, negative $B_N$ excursion would indicate that MMS crossed the magnetopause at a location where the magnetopause normal was tilted toward $-L$. The subsequent positive excursion in $B_N$ would indicate that MMS remained in the magnetosheath but crossed into a region where the magnetopause normal is tilted toward $+L$. This interpretation would agree with the motion derived using the Spatio-temporal Difference method.

The hypothesis of two sequential flux ropes offers, in our view, the most plausible explanation for the two $B_M$ enhancements and associated density minima. In this case, the motion of the magnetic structure is indicative of a primary X line being located north of the two flux ropes. The velocity of the magnetic structure increases over time, whereas the ion bulk velocity decreases. As a result, there is a mismatch of 50–100 km/s between the ion and structure velocity inside the first flux rope, while there is a better agreement between the two velocities inside the second flux rope.

This behavior is, in turn, supported by the discrepancies seen between the electric field measured by EDP and the convection electric field $-\mathbf{v_i} \times \mathbf{B}$ in the same region. As a sanity test, we compared $|\mathbf{E} + \mathbf{v_i} \times \mathbf{B}|$ and $|\mathbf{E} + \mathbf{v}_{str} \times \mathbf{B}|$. Inside the first flux rope $|\mathbf{E} + \mathbf{v}_{str} \times \mathbf{B}|$ is 50% of $|\mathbf{E} + \mathbf{v_i} \times \mathbf{B}|$, while in the second flux rope the two are of similar magnitude but with $|\mathbf{E} + \mathbf{v}_{str} \times \mathbf{B}|$ having a higher variability. Our interpretation is therefore that the discrepancy between the ion bulk velocity and structure velocity is due to ion demagnetization and not a computational artifact. Theoretical studies have shown that given the small size of our flux ropes, $<5\, d_i$, ion demagnetization is to be expected (Mandt et al., 1994).

The reversal and stagnation in $\mathbf{v}_{str,\mathbf{L}}$ observed prior to the first flux rope, combined with the increasingly negative $\mathbf{v}_{str,\mathbf{L}}$ seen in the second flux rope thus indicate that the first flux rope is compressed between the stagnation point to the south and the second, faster moving flux rope to the north. This is also consistent with the observation that the first flux rope has a smaller extent along the $L$ direction than along the $N$ direction.

The first flux rope exhibits a small, ~10% pressure increase as MMS approaches the center of the flux rope. It is worth pointing out that neither satellite passes through the center of the first flux rope. Therefore, the maximum pressure we observe is likely to be lower than the actual maximum pressure. In contrast, the second flux rope does not exhibit the pressure enhancement which is often seen near the core of a magnetic flux rope. Instead, we observe a gradual decrease in pressure throughout the second flux rope. As can be seen

in Figure 2i, MMS passes much closer to the center of the first flux rope than the center of the second flux rope. In the second flux rope, MMS appears to skim the magnetosheath edge of the flux rope. This could explain the lack of a clear pressure enhancement. In addition, starting at the interface between the two flux ropes and up until the closest approach to the center of the second flux rope, the magnetic field is closely aligned with the path of the satellite. This indicates that at this time there is little radial motion, with respect to the center of the second flux rope. This indicates that we should expect relatively small pressure gradients.

The two flux ropes were observed during very quiet magnetospheric conditions. MHD simulations have shown that magnetopause flux ropes can form even for stable solar wind conditions, due to flow shears at the subsolar point (Dorelli & Bhattacharjee, 2009). However, the flux ropes in the simulation had a size of over 1,000 km, compared to the ~300 km observed here and may represent a different type of magnetopause flux ropes. This event has similarities to that reported by Eastwood et al. (2016) in terms of the size of the flux ropes and the observation of demagnetized ions. However, the currents were significantly lower than in our first flux rope, and more similar to those observed in our second flux rope. In addition, the flux ropes reported by Eastwood et al. (2016) were force free, whereas in this event neither flux rope is force free.

Despite the quiet magnetospheric conditions, the first flux rope is very active. Inside the first flux rope we observed current reversals on the order of 3,000 nA/m$^2$ and electric fields going from being wave dominated to quasi-static, over a temporal and spatial separation of as little as 0.5 s (~2 $\omega_{ci}{}^{-1}$) and 15 km (0.5 $d_i$), respectively. This is similar to the 2–4 $\omega_{ci}{}^{-1}$ time scale observed in simulations of flux rope formation and coalescence (Drake, Swisdak, Schoeffler, et al., 2006; Zhou et al., 2014).

In contrast, the second flux rope exhibits much weaker currents and electric fields, with little or no difference observed across the MMS constellation. The lower currents observed in the second flux rope could in part be due to the fact that MMS only observed the magnetosheath edge of the flux rope, where currents are expected to be weaker than in the core. Based on the fact that the second flux rope exhibits little activity, one could argue that MMS did not encounter the flux rope proper but rather that the magnetic signatures resulted from a draping region surrounding the flux rope. However, if the magnetic signatures associated with the second flux rope were the result of field line draping only, one would not expect the population of low-energy, counterstreaming electrons to extend into the second flux rope but rather to observe an isotropic electron distribution.

Both flux ropes exhibit density depletions with the minimum density occurring around the time of the negative-positive $B_N$ reversal. It has been suggested that such density depletions are characteristic of flux ropes which have undergone coalescence (Retinò et al., 2008). In addition, 2-D PIC simulations of flux rope coalescence with a guide field has shown that newly formed secondary flux ropes were associated with an enhanced density in their core region, whereas flux ropes that have formed through coalescence exhibited density depletions (Zhou et al., 2014). However, it is not certain whether this behavior holds true in 3-D when the plasma is free to move along the principal axis of the flux rope.

We observed solitary waves both at the edges of the flux ropes as well as inside the flux ropes, which is in agreement with previous results from macroscopic and ion-scale flux ropes (Huang et al., 2016; Øieroset et al., 2014; Wilder et al., 2016). While determining the mechanism responsible for generating these solitary waves is outside the scope of this paper, we do note that they are observed both for unidirectional and bidirectional (anti-)field-aligned electron beams. Similar observations have been by the Cluster mission, but in association with magnetotail separatrices (Cattell et al., 2005). Studies have shown that solitary waves can be generated along the separatrices by a number of mechanisms such as the Buneman instability, and the electron bistream instability. (Che et al., 2010; Drake et al., 2003; Graham et al., 2016; Jara-Almonte et al., 2014; Omura et al., 1996).

The right-hand-polarized, narrowband, electromagnetic waves observed at the interface between the two flux ropes have a frequency that corresponds to 0.2–0.4 $f_{ce}$ and a propagation angle of approximately 30° with respect to the background field. These observations are consistent with obliquely propagating whistler waves. Whistler wave generation is thought to be driven either by electron temperature anisotropies, where $T_{||}/T_{\perp} < 1$ (Gary & Karimabadi, 2006), or excited by energetic electron beams (Zhang et al., 1999). In the region where we observe the whistler waves $T_{||}/T_{\perp} > 1$ indicating that the temperature anisotropy is not driving the whistler waves. However, we do observe bidirectional electrons of a few hundred eV, indicating that these whistler waves may be beam driven. These observations are similar to recent results from ion-scale

magnetosheath flux ropes, where whistler waves were observed near the edges of the flux rope (Huang et al., 2016). This supports the interpretation that the deep minimum in the in-plane magnetic field is the interface between the edges of two flux ropes rather than the core of a larger flux rope. Oblique whistler waves have also been reported along the magnetospheric separatrix of magnetopause flux ropes in conjunction with solitary wave activity (Graham et al., 2016; Wilder et al., 2016, 2017).

At the leading edge of the first flux rope, MMS 1, MMS 3, and MMS 4 observed a sharp decrease in $B_N$. In contrast, MMS 2 does not observe this sharp feature but rather a gradual decrease in $B_N$. However, it is at this point not clear whether this is a spatial effect or the result of a change in the magnetic topology. All MMS satellites observe strong, negative $J_M$, which is consistent with what one would expect to observe near a merging line.

The strong currents and electron energization observed by MMS 1, MMS 3, and MMS 4 just outside of the first flux rope, at around 03:00:13 UT, is in agreement with electrons streaming out along the separatrix from an X line located south of the satellite. In contrast, MMS 2 observes relatively weak currents on the edge of the first flux rope. Instead, a broad region of enhanced southward electron flows and positive $\mathbf{j} \cdot \mathbf{E}'$ is observed between 03:00:13.3 UT and 03:00:13.8 UT, shortly after entering the first flux rope. This could be interpreted as electrons flowing out from an X line north of MMS. Whether this electron jet is associated with the X line between the two flux ropes, or originating from a more distant X line, is not clear. However, the absence of such an electron jet in the data from MMS 1, MMS 3, and MMS 4, as well as the lack of activity at the interface between the two flux ropes, suggests the latter.

The interface between the two flux ropes exhibits a deep minimum in the in-plane components of the magnetic field, where $\sqrt{{B_N}^2 + {B_L}^2} < 2$ nT. Both flux ropes exhibit an asymmetric bipolar $B_N$ signature, being weaker at the interface between the two flux ropes. When combined, they give the appearance of a quadrupolar $B_N$ signature across the two flux ropes. Similar signatures have been reported at the interface between macroscopic flux ropes, interpreted as the result of dissipation of magnetic energy caused by flux rope coalescence (Zhou et al., 2017). Alternatively, asymmetric $B_N$ signatures similar to those observed here can arise from an oblique crossing of a flux rope (Farrugia et al., 1987). However, this model cannot reproduce both asymmetric $B_N$ signatures for the observed $B_L$ nor explain the deep in-plane null observed between the flux ropes. The in-plane minimum is most pronounced for MMS 2 where $\sqrt{{B_N}^2 + {B_L}^2} = 0.1$ nT. This is in agreement with the position of MMS 2 relative to the other satellites and is most likely not due to temporal variations. Since the motion analysis shows that the two flux ropes are converging, rather than diverging, and that we either observe a current reversal with a negative $J_M$ of approximately 700 nA/m$^2$ (MMS 1, MMS 3, and MMS 4) or an extremely weak but positive $J_M$ (MMS 2), we draw the conclusion that the null located at the interface between the two flux ropes is likely to be associated with a merging line.

The negative $J_L$ spikes observed by MMS 1, MMS 3, and MMS 4 near the center of the first flux rope indicate electrons flowing from the first flux rope toward the second flux rope. In this case $\mathbf{J} \cdot \mathbf{E}' < 0$ which suggests that the electron flow is pressure driven rather than driven by the electric fields. This in agreement with what one would expect if compression of the first flux rope is causing plasma to leak out along recently opened field lines. MMS 4 observes a narrow spike in the current, which would indicate that at that time only a few field lines were open. In contrast, MMS 1 and MMS 3 observe a much broader spike, indicating that more field lines have opened. The lower peak current could indicate that plasma of the two flux ropes is starting to reach an equilibrium. In contrast, MMS 2 observes no such current spike, indicating that the coalescence process has stopped or slowed down, which explains why we see little current and no energy conversion occurring near the in-plane null. In addition, if the spike in $J_L$ was caused by an increase in the azimuthal current, due to flux rope being compressed, we would expect to see this increase occurring simultaneously throughout the flux rope, and not as a localized phenomenon.

## 5. Conclusions

Our interpretation of the event, summarized in Figure 8, is that the rapid changes observed inside the first flux rope, from one satellite to another, is due to flux rope coalescence occurring at the edges of the first flux rope. However, there is no data indicating that MMS encountered the electron diffusion region in either case.

In contrast to the leading edge of the first flux rope, the interface between the two flux ropes exhibits no strong electric fields, electron jets or energy conversion, indicating that the coalescence either occurred

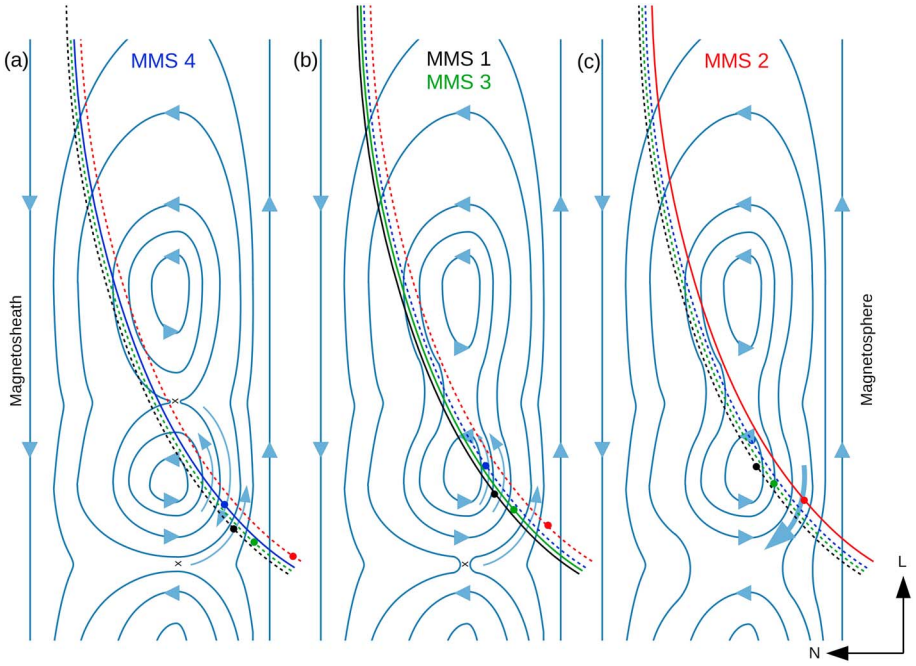


**Figure 8.** Cartoon illustrating the evolution of the two flux ropes as seen by the different MMS satellites. (a) MMS 4, (b) MMS 1 and MMS 3, and (c) MMS 4. The blue arrows indicate the electron jets.

at an earlier time or that the process is extremely slow. The two flux ropes have a ~14 degree offset between their principal axes, which combined with the large guide field leads to a lower magnetic shear at the interface between the flux ropes. This could result in a decreased reconnection rate. However, it is worth noting that any current modulations due to the 200–400 Hz whistler waves would be washed out due to the 30 ms time resolution of FPI. The time scale over which we observe the large current and electric field reversals is ~0.5 s (~2 $\omega_{ci}^{-1}$) is which is similar to the 2–4 $\omega_{ci}^{-1}$ time scale reported from simulations of flux rope formation and coalescence (Drake, Swisdak, Schoeffler, et al., 2006; Zhou et al., 2014).

Given the complex 3-D topology and short time scales, we can at this point neither draw any definitive conclusions on the connectivity of individual field lines nor fully differentiate between spatial and temporal variations. Fully characterizing and understanding these 3-D, non-force-free flux ropes, their high time variability and non-MHD ion properties will likely require extensive modeling efforts and is outside the scope of this paper.

**Acknowledgments**
This paper was made possible by the hard work of the MMS Team. All data are publicly available at MMS Science Data Center (https://lasp.colorado.edu/mms/sdc/public/). This work was supported by NASA via contract 499878Q.

## References

Burch, J., Moore, T., Torbert, R., & Giles, B. (2016). Magnetospheric Multiscale overview and science objectives. *Space Science Reviews*, *199*(1–4), 5–21.

Cattell, C., Dombeck, J., Wygant, J., Drake, J. F., Swisdak, M., Goldstein, M. L., … Balogh, A. (2005). Cluster observations of electron holes in association with magnetotail reconnection and comparison to simulations. *Journal of Geophysical Research*, *110*, A01211. https://doi.org/10.1029/2004JA010519

Che, H., Drake, J. F., Swisdak, M., & Yoon, P. H. (2010). Electron holes and heating in the reconnection dissipation region. *Geophysical Research Letters*, *37*, L11105. https://doi.org/10.1029/2010GL043608

Chen, L.-J., Bhattacharjee, A., Puhl-Quinn, P. A., Yang, H., Bessho, N., Imada, S., … Georgescu, E. (2008). Observation of energetic electrons within magnetic islands. *Nature Physics*, *4*(1), 19–23. https://doi.org/10.1038/nphys777

Cowley, S. (1982). The causes of convection in the Earth's magnetosphere: A review of developments during the IMS. *Reviews of Geophysics*, *20*(3), 531–565.

Daughton, W., Roytershteyn, V., Karimabadi, H., Yin, L., Albright, B. J., Bergen, B., & Bowers, K. J. (2011). Role of electron physics in the development of turbulent magnetic reconnection in collisionless plasmas. *Nature Physics*, *7*(7), 539–542. https://doi.org/10.1038/nphys1965

Daughton, W., Scudder, J., & Karimabadi, H. (2006). Fully kinetic simulations of undriven magnetic reconnection with open boundary conditions. *Physics of Plasmas*, *13*(7), 072101. https://doi.org/10.1063/1.2218817

Dong, X.-C., Dunlop, M., Trattner, K., Phan, T., Fu, H.-S., & Cao, J.-B. (2017). Structure and evolution of flux transfer events near dayside magnetic reconnection dissipation region: MMS observations. *Geophysical Research Letters*, *44*, 5951–5959. https://doi.org/10.1002/2017GL073411

Dorelli, J., & Bhattacharjee, A. (2009). On the generation and topology of flux transfer events. *Journal of Geophysical Research*, *114*, A06213. https://doi.org/10.1029/2008JA013410

Drake, J. F., Swisdak, M., Cattell, C., Shay, M. A., Rogers, B. N., & Zeiler, A. (2003). Formation of electron holes and particle energization during magnetic reconnection. *Science*, *299*(5608), 873–877. https://doi.org/10.1126/science.1080333

Drake, J. F., Swisdak, M., Che, H., & Shay, M. A. (2006). Electron acceleration from contracting magnetic islands during reconnection. *Nature*, *443*(7111), 553–556. https://doi.org/10.1038/nature05116

Drake, J. F., Swisdak, M., Schoeffler, K. M., Rogers, B. N., & Kobayashi, S. (2006). Formation of secondary islands during magnetic reconnection. *Geophysical Research Letters*, *33*, L13105. https://doi.org/10.1029/2006GL025957

Eastwood, J., Phan, T., Cassak, P., Gershman, D., Haggerty, C., Malakit, K., … Wang, S. (2016). Ion-scale secondary flux ropes generated by magnetopause reconnection as resolved by MMS. *Geophysical Research Letters*, *43*, 4716–4724. https://doi.org/10.1002/2016GL068747

Ergun, R. E., Tucker, S., Westfall, J., Goodrich, K. A., Malaspina, D. M., Summers, D., … Cully, C. M. (2016). The axial double probe and fields signal processing for the MMS mission. *Space Science Reviews*, *199*, 167–188. https://doi.org/10.1007/s11214-014-0115-x

Farrugia, C., Elphic, R., Southwood, D., & Cowley, S. (1987). Field and flow perturbations outside the reconnected field line region in flux transfer events: Theory. *Planetary and Space Science*, *35*(2), 227–240. https://doi.org/https://doi.org/10.1016/0032-0633(87)90091-2

Fear, R. C., Milan, S. E., Fazakerley, A. N., Lucek, E. A., Cowley, S. W. H., & Dandouras, I. (2008). The azimuthal extent of three flux transfer events. *Annales Geophysicae*, *26*(8), 2353–2369. https://doi.org/10.5194/angeo-26-2353-2008

Fermo, R. L., Drake, J. F., Swisdak, M., & Hwang, K.-J. (2011). Comparison of a statistical model for magnetic islands in large current layers with hall MHD simulations and cluster FTE observations. *Journal of Geophysical Research*, *116*, A09226. https://doi.org/10.1029/2010JA016271

Fermo, R. L., Drake, J. F., & Swisdak, M. (2012). Secondary magnetic islands generated by the Kelvin-Helmholtz instability in a reconnecting current sheet. *Physical Review Letters*, *108*, 255005. https://doi.org/10.1103/PhysRevLett. 108.255005

Gary, S. P., & Karimabadi, H. (2006). Linear theory of electron temperature anisotropy instabilities: Whistler, mirror, and Weibel. *Journal of Geophysical Research*, *111*, A11224. https://doi.org/10.1029/2006JA011764

Graham, D. B., Khotyaintsev, Y. V., Vaivads, A., & André, M. (2016). Electrostatic solitary waves and electrostatic waves at the magnetopause. *Journal of Geophysical Research: Space Physics*, *121*, 3069–3092. https://doi.org/10.1002/2015JA021527

Haaland, S., Sonnerup, B. Ö., Dunlop, M., Balogh, A., Georgescu, E., & Hasegawa, H. (2004). Four-spacecraft determination of magnetopause orientation, motion and thickness: Comparison with results from single-spacecraft methods. *Annales Geophysicae*, *22*, 1347–1365.

Huang, S., Sahraoui, F., Retino, A., Le Contel, O., Yuan, Z., Chasapis, A., … Burch, J. L. (2016). MMS observations of ion-scale magnetic island in the magnetosheath turbulent plasma. *Geophysical Research Letters*, *43*, 7850–7858. https://doi.org/10.1002/2016GL070033

Jara-Almonte, J., Daughton, W., & Ji, H. (2014). Debye scale turbulence within the electron diffusion layer during magnetic reconnection. *Physics of Plasmas*, *21*(3), 032114. https://doi.org/10.1063/1.4867868

Karimabadi, H., Daughton, W., & Scudder, J. (2007). Multi-scale structure of the electron diffusion region. *Geophysical Research Letters*, *34*, L13104. https://doi.org/10.1029/2007GL030306

Le Contel, O., Leroy, P., Roux, A., Coillot, C., Alison, D., Bouabdellah, A., … de la Porte, B. (2016). The search-coil magnetometer for MMS. *Space Science Reviews*, *199*(1), 257–282. https://doi.org/10.1007/s11214-014-0096-9

Lee, L. C., & Fu, Z. F. (1985). A theory of magnetic flux transfer at the Earth's magnetopause. *Geophysical Research Letters*, *12*(2), 105–108. https://doi.org/10.1029/GL012i002p00105

Lindqvist, P.-A., Olsson, G., Torbert, R. B., King, B., Granoff, M., Rau, D., … Tucker, S. (2016). The spin-plane double probe electric field instrument for MMS. *Space Science Reviews*, *199*(1), 137–165. https://doi.org/10.1007/s11214-014-0116-9

Mandt, M. E., Denton, R. E., & Drake, J. F. (1994). Transition to whistler mediated magnetic reconnection. *Geophysical Research Letters*, *21*(1), 73–76. https://doi.org/10.1029/93GL03382

Maynard, N. C., Farrugia, C. J., Burke, W. J., Ober, D. M., Mozer, F. S., Rème, H., … Siebert, K. D. (2012). Cluster observations of the dusk flank magnetopause near the sash: Ion dynamics and flow-through reconnection. *Journal of Geophysical Research*, *117*, A10201. https://doi.org/10.1029/2012JA017703

Øieroset, M., Sundkvist, D., Chaston, C. C., Phan, T. D., Mozer, F. S., McFadden, J. P., … Eastwood, J. P. (2014). Observations of plasma waves in the colliding jet region of a magnetic flux rope flanked by two active X lines at the subsolar magnetopause. *Journal of Geophysical Research: Space Physics*, *119*, 6256–6272. https://doi.org/10.1002/2014JA020124

Omura, Y., Matsumoto, H., Miyake, T., & Kojima, H. (1996). Electron beam instabilities as generation mechanism of electrostatic solitary waves in the magnetotail. *Journal of Geophysical Research*, *101*(A2), 2685–2697. https://doi.org/10.1029/95JA03145

Paschmann, G., & Daly, P. W. (1998). *Analysis methods for multi-spacecraft data* (1.1 edn.). Noordwjik, Netherlands: ESA Publications Division.

Paschmann, G., & Daly, P. W. (2008). *Multi-spacecraft analysis methods revisited*. Noordwijk, Netherlands: ESA Publications Division.

Paschmann, G., Haerendel, G., Papamastorakis, I., Sckopke, N., Bame, S. J., Gosling, J. T., & Russell, C. T. (1982). Plasma and magnetic field characteristics of magnetic flux transfer events. *Journal of Geophysical Research*, *87*(A4), 2159–2168. https://doi.org/10.1029/JA087iA04p02159

Pollock, C., Moore, T., Jacques, A., Burch, J., Gliese, U., Saito, Y., … Zeuch, M. (2016). Fast plasma investigation for Magnetospheric Multiscale. *Space Science Reviews*, *199*(1), 331–406. https://doi.org/10.1007/s11214-016-0245-4

Retinò, A., Nakamura, R., Vaivads, A., Khotyaintsev, Y., Hayakawa, T., Tanaka, K., … Cornilleau-Wehrlin, N. (2008). Cluster observations of energetic electrons and electromagnetic fields within a reconnecting thin current sheet in the Earth's magnetotail. *Journal of Geophysical Research*, *113*, A12215. https://doi.org/10.1029/2008JA013511

Russell, C. T., Anderson, B. J., Baumjohann, W., Bromund, K. R., Dearborn, D., Fischer, D., … Richter, I. (2016). The Magnetospheric Multiscale magnetometers. *Space Science Reviews*, *199*(1), 189–256. https://doi.org/10.1007/s11214-014-0057-3

Russell, C. T., & Elphic, R. C. (1978). Initial ISEE magnetometer results: Magnetopause observations. *Space Science Reviews*, *22*(6), 681–715. https://doi.org/10.1007/BF00212619

Scudder, J., Holdaway, R., Glassberg, R., & Rodriguez, S. (2008). Electron diffusion region and thermal demagnetization. *Journal of Geophysical Research*, *113*, A10208. https://doi.org/10.1029/2008JA013361

Shi, Q. Q., Shen, C., Dunlop, M. W., Pu, Z. Y., Zong, Q.-G., Liu, Z. X., … Balogh, A. (2006). Motion of observed structures calculated from multi-point magnetic field measurements: Application to cluster. *Geophysical Research Letters*, *33*, L08109. https://doi.org/10.1029/2005GL025073

Shi, Q. Q., Shen, C., Pu, Z. Y., Dunlop, M. W., Zong, Q.-G., Zhang, H., … Balogh, A. (2005). Dimensional analysis of observed structures using multipoint magnetic field measurements: Application to cluster. *Geophysical Research Letters*, *32*, L12105. https://doi.org/10.1029/2005GL022454

Sonnerup, B. U. O. (1987). On the stress balance in flux transfer events. *Journal of Geophysical Research*, *92*(A8), 8613–8620. https://doi.org/10.1029/JA092iA08p08613

Torbert, R., Russell, C., Magnes, W., Ergun, R., Lindqvist, P.-A., LeContel, O., … Lappalainen, K. (2016). The fields instrument suite on MMS: Scientific objectives, measurements, and data products. *Space Science Reviews*, *199*(1–4), 105–135.

Uzdensky, D. A., Loureiro, N. F., & Schekochihin, A. A. (2010). Fast magnetic reconnection in the plasmoid-dominated regime. *Physical Review Letters*, *105*, 235002. https://doi.org/10.1103/PhysRevLett.105.235002

Wang, R., Lu, Q., Nakamura, R., Huang, C., Du, A., Guo, F., … Wang, S. (2016). Coalescence of magnetic flux ropes in the ion diffusion region of magnetic reconnection. *Nature Physics*, *12*(3), 263–267.

Wilder, F., Ergun, R., Goodrich, K., Goldman, M., Newman, D., Malaspina, D., … Holmes, J. C. (2016). Observations of whistler mode waves with nonlinear parallel electric fields near the dayside magnetic reconnection separatrix by the Magnetospheric Multiscale mission. *Geophysical Research Letters*, *43*, 5909–5917. https://doi.org/10.1002/2016GL069473

Wilder, F. D., Ergun, R. E., Newman, D. L., Goodrich, K. A., Trattner, K. J., Goldman, M. V., … Lindqvist, P.-A. (2017). The non-linear behaviour of whistler waves at the reconnecting dayside magnetopause as observed by the Magnetospheric Multiscale mission: A case study. *Journal of Geophysical Research: Space Physics*, *122*, 5487–5501. https://doi.org/10.1002/2017JA024062

Zenitani, S., Hesse, M., Klimas, A., Black, C., & Kuznetsova, M. (2011). The inner structure of collisionless magnetic reconnection: The electron-frame dissipation measure and hall fields. *Physics of Plasmas*, *18*(12), 122108.

Zhang, Y., Matsumoto, H., & Kojima, H. (1999). Whistler mode waves in the magnetotail. *Journal of Geophysical Research*, *104*(A12), 28,633–28,644. https://doi.org/10.1029/1999JA900301

Zhou, M., Berchem, J., Walker, R., El-Alaoui, M., Deng, X., Cazzola, E., … Burch, J. L. (2017). Coalescence of macroscopic flux ropes at the subsolar magnetopause: Magnetospheric Multiscale observations. *Physical Review Letters*, *119*(5), 055101.

Zhou, M., Pang, Y., Deng, X., Huang, S., & Lai, X. (2014). Plasma physics of magnetic island coalescence during magnetic reconnection. *Journal of Geophysical Research: Space Physics*, *119*, 6177–6189. https://doi.org/10.1002/2013JA019483